


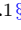


A χ^2 statistic for the identification of strongly lensed gravitational waves from compact binary coalescences

Sudhir Gholap¹^{*}, Kanchan Soni^{2,1}[†], Shasvath J. Kapadia¹[‡], and Sanjeev Dhurandhar¹[§]
¹*Inter University Centre for Astronomy and Astrophysics, Post Bag 4, Ganeshkhind, Pune 411007 and*
²*Department of Physics, Syracuse University, Crouse Dr, Syracuse, NY 13210*

(Dated: February 4, 2025)

Gravitational waves (GWs) emanated by stellar mass compact binary coalescences (CBCs), and lensed by galaxy- or cluster-scale lenses, will produce two or more copies of the GW signal. These will have identical phase evolution but differing amplitudes. Such lensing signatures are expected to be detected by the end of the LIGO-Virgo-Kagra's (LVK's) fifth observing run (O5). In this work, we propose a novel χ_{lens}^2 statistic to segregate pairs of detected GW events as either lensed or unlensed, using templates typically used in GW searches. The statistic is an application of the generalized χ^2 discriminator described in Dhurandhar *et al.* [1], tailored to probe the similarity (or lack thereof) between the phase evolutions of two CBC signals. We assess the performance of χ_{lens}^2 on a realistic astrophysical dataset of lensed and unlensed CBCs detectable in O4, assuming a single LIGO-like detector at design sensitivity. We find that we can correctly identify lensed events with efficiencies comparable to existing Bayesian and machine learning methods. Evaluating χ_{lens}^2 is orders of magnitude faster than Bayesian methods. Moreover, the statistics of χ_{lens}^2 , in stationary Gaussian noise, are fully understood, in contrast to machine learning methods. χ_{lens}^2 can, therefore, be used to rapidly and accurately weed out the vast majority of unlensed candidate pairs and identify lensed pairs.

Keywords: Gravitational Waves, Gravitational Lensing, Compact Binaries

I. INTRODUCTION

The LIGO-Virgo [2, 3] network of gravitational-wave (GW) detectors has observed ~ 90 compact binary coalescence (CBC) events in its first three observing runs (O1, O2, O3) [4]. Additional events were independently catalogued in [5–9] using the publicly accessible LIGO-Virgo data [10, 11]. The overwhelming majority of these are binary black holes (BBHs). Nevertheless, binary neutron star [12, 13] and neutron star black hole mergers [14] have also been observed. The ongoing O4 is likely to more than triple the number of detections, confirming that GW astronomy has well and truly arrived.

The detected CBCs have enabled some of the most unique tests of general relativity (GR) in the strong field regime [15]. These include: a residuals test where the best fit GR waveform is subtracted out from the data, and the consistency of the residual with noise is assessed [16–18]; an inspiral-merger-ringdown consistency test, where source parameters extracted from low and high-frequency parts of the signal, assuming a GR template waveform, are compared [19, 20]; a test that looks for deviations in Post Newtonian coefficients of the GW signal as a means to investigate the consistency of the

inspiral with GR [21–28]; and propagation tests that compare the speed of GWs with the speed of light [29], and look for signatures of velocity dispersion due to a non-zero graviton mass [30].

Gravitational lensing of GWs promises to provide yet another unique test of GR. This phenomenon occurs when GWs encounter large agglomerations of matter. In particular, when GWs from stellar mass CBCs encounter galaxies or clusters, strong lensing in the geometric optics regime will ensue. As a result, multiple temporally resolved copies of the source GW signal will be observed by the GW detector network, with image time delays that span minutes to months for galaxy-scale lenses [31–33], and weeks to years for cluster-scale lenses [34–38]. These copies will have identical phase evolutions, but differing amplitudes (due to (de)magnification) as well as a constant phase difference of 0 , $\pi/2$, or π (known as the Morse phase) [39–41]. On the other hand, if these GWs encounter lenses, such as intermediate-mass black holes, whose Schwarzschild radii are comparable to the wavelength of the GWs, a single modulated GW image will be produced, exhibiting interference, diffraction and beating patterns [42–49]. Gravitational lensing will enable additional powerful tests of GR [50–54]; provide precise measurements of cosmological parameters [55–61]; drastically enhance GW early warning [62]; enable constraints on the fraction of dark matter as massive compact halo objects [63, 64], as well as on the mass of the warm dark matter particle [65]; probe properties of the lens such as electric charge [66], and probe the proper motion of iso-

* sudhir.gholap@iucaa.in

† ksoni01@syr.edu

‡ shasvath.kapadia@iucaa.in

§ sanjeev@iucaa.in

lated Galactic neutron stars [67].

The LVK has conducted multiple searches for signatures of GW lensing in its first three observing runs. However, no confirmed detection of the gravitational lensing of GWs has been reported [68–70]. Based on lensing rate estimates, it is expected that the first detection of strongly lensed GWs will occur before the end of O5 [71, 72]. In anticipation of this exciting possibility, a number of search methods have been proposed. These include:

- A posterior overlap statistic that measures the degree of overlap between posteriors of source parameters, inferred from the data surrounding each of the events in a candidate pair [73]. An upgrade to this statistic, by self-consistently incorporating prior astrophysical information, was recently provided [74].
- A machine learning (ML) based method that uses time-frequency maps and localization skymaps of the candidate pair to provide a probability of class membership (lensed or unlensed) [75, 76].
- An approximate method that combines localization skymaps with the Bhattacharya distance between detector-frame mass posteriors, approximated as Gaussians, of the two events in a candidate pair [77].
- A method that compares the GW phase of the two events in the pair at a fixed reference frequency [78], and another that cross correlates data surrounding each of the events in the pair [79].
- Comprehensive Bayesian methods that construct a joint likelihood from the data surrounding each of the events in the candidate pair [80–84].

Each of these methods has its unique strengths and shortcomings. For example, the posterior overlap statistic, as well as the comprehensive Bayesian methods, are expected to be optimal in stationary Gaussian noise, but they require large-scale parameter estimation runs that could take anywhere from hours to weeks, per event candidate pair¹. On the other hand, rapid methods such as ones that use ML require carefully constructed training sets, and the behavior of the ML algorithm is not always fully understood. The approximate method mentioned above, while rapid, suffers from the fact that

the Gaussian approximation to the posterior may not be valid in real noise for low-significance events.

In this work, we propose a template-based method to rapidly identify a pair of events as either lensed or unlensed. The method applies the generalized χ^2 statistic proposed in Dhurandhar *et al.* [1] and tunes it to assess the phase-evolution-consistency between quasicircular and quadrupolar GW signals in a candidate lensed pair². In particular, using the trigger template, as well as neighboring ones associated with the louder of the two events in a candidate pair, a vector space orthogonal to this neighborhood is constructed. The strain data pertaining to the second (weaker) signal is then projected onto the orthogonal vector space.

In the absence of noise, a lensed pair would yield a zero projection, while an unlensed pair would yield a projection proportional to the second event’s signal-to-noise ratio (SNR) squared. In the presence of stationary Gaussian noise, the projection for the lensed pair will be a χ^2 random variable, whose mean will depend on the number of degrees of freedom of χ^2 . On the other hand, for an unlensed pair, the mean will depend on the SNR-squared, in addition to the degrees of freedom.

We assess the performance of χ_{lens}^2 on a realistic astrophysical dataset consisting of lensed and unlensed pairs in a ratio of approximately 1 : 1600. These are injected in Gaussian noise, assuming an O4-like (design sensitivity) power spectral density (PSD), as well as a single detector configuration, ensuring that the weaker signal in the candidate pair has an $\text{SNR} \geq 8$. We find that we are able to segregate lensed and unlensed pairs with an efficiency (true positive rate), at a low false positive rate, comparable to the posterior overlap statistic. Moreover, we study the performance of χ_{lens}^2 as a function of the SNR of the candidate pairs, as well as their duration within the sensitivity band of the detector. As expected, we find that increasing SNR and in-band duration improves the performance of χ_{lens}^2 . Our work therefore provides an accurate, rapidly calculable, and readily interpretable statistic for the identification of strongly lensed pairs of GWs.

The rest of the paper is organized as follows. Section II provides a summary of the posterior overlap statistic, as well as details on the generalized χ^2 and χ_{lens}^2 statistics. Section III describes the construction of the χ_{lens}^2 statistic developed in this work and examines its properties. Section IV outlines the results demonstrating the performance of χ_{lens}^2 . Finally, Section V summarizes the paper and discusses the scope for future work.

¹ It may be argued that the posterior overlap statistic uses existing posteriors on the individual detected GW events and does not require a separate large-scale parameter estimation run. Nevertheless, not all GW events have PE posteriors readily available, such as subthreshold events.

² The generalized χ^2 was also used in the context of segregating signals from glitches in [85].

II. METHODS

We describe, in detail, the construction of χ_{lens}^2 as an application of the generalized χ^2 statistic. We provide a geometric interpretation of this discriminator and provide a robust derivation of the expected foreground and background distributions of χ_{lens}^2 in stationary Gaussian noise. We also briefly summarize the posterior overlap statistic, which will serve as the benchmark for comparison with χ_{lens}^2 .

A. The Posterior Overlap Statistic

Consider a detector strain time series $x(t)$, containing a GW signal $A\hat{h}^s(t, \vec{\theta})$ with amplitude A , source parameters $\vec{\theta}$, and noise $n(t)$. The noise $n(t)$ is usually modeled as a realization of stationary Gaussian noise with zero mean and a power spectral density $S_n(f)$. The strain is then a simple superposition of the two,

$$x(t) = n(t) + A\hat{h}^s(t, \vec{\theta}). \quad (1)$$

The presence of $A\hat{h}^s(t, \vec{\theta})$ in $x(t)$ is probed by evaluating the matched-filter SNR $\rho = (x|\hat{h}^t)$. Here, \hat{h}^t is a normalized GW template, and inner product $(\cdot|\cdot)$ is defined as

$$(a|b) = 4 \text{Re} \int_{f_{\min}}^{f_{\max}} \frac{\tilde{a}^*(f)\tilde{b}(f)}{S_n(f)} df, \quad (2)$$

where $a(t)$ and $b(t)$ are two time series, and \tilde{a} and \tilde{b} are their Fourier transforms. If \hat{h}^t is an exact representation of the signal in the data $\hat{h}^s(t, \vec{\theta})$, then, ρ , on average, will equal the so-called optimal SNR $\langle \rho \rangle = \rho_{\text{opt}} = (A\hat{h}^s|\hat{h}^t) = A$.

Inferring the parameters $\vec{\theta}$ requires extensive parameter estimation runs. During these runs, the GW posterior distribution is sampled

$$p(\vec{\theta}|x) = \frac{p(\vec{\theta})p(x|\vec{\theta})}{p(x)}, \quad (3)$$

where $p(x|\vec{\theta}) \propto \exp[-(x - A\hat{h}^t|x - A\hat{h}^t)/2]$ is the likelihood, $p(\vec{\theta})$ is the prior, and $p(x)$ is a normalisation constant called the evidence.

The posterior overlap statistic acts as a discriminator between lensed and unlensed candidate pairs of detected GW events. The discriminator exploits the fact that lensed events will have identical phase evolutions, and therefore, their intrinsic parameters in the detector frame must be identical. Consequently, the degree of

overlap between the posteriors of the intrinsic parameters of the two events could be indicative of the lensed nature of the pair.

Formally, the posterior overlap statistic is defined as follows. Consider two data streams $x_1(t)$ and $x_2(t)$, known to contain GW signals $A_1\hat{h}^{s_1}(t)$ and $A_2\hat{h}^{s_2}(t)$, respectively. Let \mathcal{H}_L be the hypothesis that $A_{1,2}\hat{h}^{s_{1,2}}(t)$ are lensed copies, and let \mathcal{H}_U be the hypothesis that the two signals are unrelated (i.e., unlensed). Assuming no prior information on which hypothesis is preferred, an optimal Bayesian discriminator can be constructed from the ratio of the evidences of the joint data set $\{x_1(t), x_2(t)\}$ conditioned on each of the two hypotheses [73]

$$\mathcal{B}_U^L = \frac{p(x_1, x_2 | \mathcal{H}_L)}{p(x_1, x_2 | \mathcal{H}_U)} = \int \frac{p(\vec{\theta} | x_1)p(\vec{\theta} | x_2)}{p(\vec{\theta})} d\vec{\theta}. \quad (4)$$

The posterior overlap statistic [73] is then simply a Bayes factor, which can be constructed using the individual intrinsic parameter posteriors of the two GW events and the prior used in the construction of the posteriors.

B. The Unified χ^2 Discriminator

The general framework for χ^2 discriminators has been described in Dhurandhar *et al.* [1], where various χ^2 discriminators are unified into a single discriminator, which can be appropriately termed as the *unified* χ^2 . In this framework, a data stream $x(t)$ defined over a time interval $[0, T]$ is viewed as a vector \mathbf{x} denoted in boldface. Such data streams form a vector space \mathcal{D} of large number of dimensions equal to the number of sample points in the data stream. The scalar product, defined in Eq. (2), turns this space into a Hilbert space. The detector noise $n(t)$ is a stochastic process defined over the time segment $[0, T]$. A specific noise realization is a vector $\mathbf{n} \in \mathcal{D}$. In general, \mathbf{n} is a random vector; we assume that it has an ensemble mean zero and is stationary in the wide sense.

The χ^2 discriminator maps a vector in \mathcal{D} to a positive real number. It is defined so that its value on the signal is zero and, in Gaussian noise, has a χ^2 distribution with a reasonable number of degrees of freedom, p . If a template \mathbf{h} is triggered, then the χ^2 for \mathbf{h} is defined by choosing a finite-dimensional subspace \mathcal{S} of dimension p that is orthogonal to \mathbf{h} , i.e., for any $\mathbf{y} \in \mathcal{S}$, we must have $(\mathbf{y}|\mathbf{h}) = 0$. Then the χ^2 for the template \mathbf{h} is defined as just the square of the L_2 norm of the data vector \mathbf{x} projected onto \mathcal{S} . Specifically, we perform the following operations. Take a data vector $\mathbf{x} \in \mathcal{D}$ and decompose it as

$$\mathbf{x} = \mathbf{x}_S + \mathbf{x}_{S^\perp}, \quad (5)$$

where \mathcal{S}^\perp is the orthogonal complement of \mathcal{S} in \mathcal{D} . $\mathbf{x}_\mathcal{S}$ and $\mathbf{x}_{\mathcal{S}^\perp}$ are projections of \mathbf{x} into the subspaces \mathcal{S} and \mathcal{S}^\perp , respectively. We may write \mathcal{D} as a direct sum of \mathcal{S} and \mathcal{S}^\perp , that is, $\mathcal{D} = \mathcal{S} \oplus \mathcal{S}^\perp$. Then the required statistic χ^2 is,

$$\chi^2(\mathbf{x}) = \|\mathbf{x}_\mathcal{S}\|^2. \quad (6)$$

The χ^2 statistic so defined has the following properties. Given any orthonormal basis of \mathcal{S} , say \mathbf{e}_α , with $\alpha = 1, 2, \dots, p$ and $(\mathbf{e}_\alpha | \mathbf{e}_\beta) = \delta_{\alpha\beta}$, we obtain the following:

1. For a general data vector $\mathbf{x} \in \mathcal{D}$, we have

$$\chi^2(\mathbf{x}) = \|\mathbf{x}_\mathcal{S}\|^2 = \sum_{\alpha=1}^p |(\mathbf{x} | \mathbf{e}_\alpha)|^2. \quad (7)$$

2. Clearly, $\chi^2(\mathbf{h}) = 0$ because the projection of \mathbf{h} onto the subspace \mathcal{S} is zero, i.e., $\mathbf{h}_\mathcal{S} = 0$.
3. Now, the noise \mathbf{n} is taken to be stationary and Gaussian, with PSD $S_n(f)$ and mean zero. Therefore, the following relation is valid:

$$\chi^2(\mathbf{n}) = \|\mathbf{n}_\mathcal{S}\|^2 = \sum_{\alpha=1}^p |(\mathbf{n} | \mathbf{e}_\alpha)|^2. \quad (8)$$

The random variables $(\mathbf{n} | \mathbf{e}_\alpha)$ are independent and Gaussian distributed, with zero mean and unit variance. This is because $\langle (\mathbf{e}_\alpha | \mathbf{n})(\mathbf{n} | \mathbf{e}_\beta) \rangle = (\mathbf{e}_\alpha | \mathbf{e}_\beta) = \delta_{\alpha\beta}$, where the angular brackets denote ensemble average (see [86] for proof). Thus, $\chi^2(\mathbf{n})$ possesses a χ^2 distribution with p degrees of freedom.

One is free to choose any orthonormal basis of \mathcal{S} . In an orthonormal basis, the statistic is manifestly χ^2 since it can be written as a sum of squares of independent Gaussian random variables, with mean zero and variance unity.

In the context of CBC searches, however, we have a family of waveforms that depends on a set of parameters $\vec{\Theta}$. These include intrinsic parameters, $\vec{\theta}$, such as the masses and spins of the binary components, as well as kinematical parameters, such as the phase and time of coalescence. The templates corresponding to these waveforms are normalized, i.e., $\|\mathbf{h}(\vec{\Theta})\| = 1$. Then the templates trace out a submanifold \mathcal{P} of \mathcal{D} , called the *signal manifold*. We now associate a p -dimensional subspace \mathcal{S} orthogonal to the template $\mathbf{h}(\vec{\Theta})$ at each point of \mathcal{P} . Thus, we have a p -dimensional vector space ‘‘attached’’ to each point of \mathcal{P} . When done smoothly, this construction results in a vector bundle. We have, therefore, found a very general mathematical structure for the χ^2 discriminator. It is easily shown that the traditional χ^2 discriminator [87] falls under the class of *unified* χ^2 [1].

A waveform could have an arbitrary phase in the time domain, which can be written as a linear combination of two orthogonal templates \mathbf{h}_0 and $\mathbf{h}_{\pi/2}$. In the Fourier domain, these two waveforms are simply related by a factor of the complex number i . Taking only the positive frequency components contains full information of the real data, and this is explicitly shown in Appendix A. The complex approach is useful because the waveforms span a 2-dimensional space parametrized by the coalescence phase. We, therefore, consider only the positive frequency part $f > 0$ of the signal as well as of the data. This gives us complex vectors that again belong to a Hilbert space \mathcal{H} , which is essentially, $L^2[f_{\min}, f_{\max}]$ with a weighted measure defined by $d\mu = df/S_n(f)$. On \mathcal{H} , we define the scalar product as

$$(\mathbf{x}, \mathbf{y}) = 4 \int_{f_{\min}}^{f_{\max}} \frac{\tilde{x}^*(f) \tilde{y}(f)}{S_n(f)} df. \quad (9)$$

We have scaled the usual scalar product by a factor of 4 so that the norms of any vector as computed by either scalar product agree. This is shown in Eq. (A3) in Appendix A. The scalar product in Eq. (9) is related in a simple way to the one defined in Eq. (2). In Appendix A, this relation is explicitly deduced. The scalar product is complex in general, satisfying $(\mathbf{y}, \mathbf{x}) = (\mathbf{x}, \mathbf{y})^*$, which means the order of the vectors appearing in the scalar product is important and must be taken into account while performing computations. We assert that \mathcal{H} is isomorphic to \mathcal{D} . The entire procedure for constructing the χ^2 can be followed through as in the case of \mathcal{D} , where now we deal with complex vectors and use the scalar product as defined by Eq. (9). The resulting χ^2 is, of course, real and positive, although it has an even number of (real) degrees of freedom.

III. χ_{lens}^2 : CONSTRUCTION, PROPERTIES AND INTERPRETATION

A. The recipe

In the context of strong-lensing, consider two strain data segments \mathbf{x}_1 and \mathbf{x}_2 , containing signals $\hat{\mathbf{h}}^{\text{s1}}$ and $\hat{\mathbf{h}}^{\text{s2}}$, with amplitudes A_1 and A_2 ($A_1 > A_2$) respectively and buried in Gaussian noise \mathbf{n} . Then we have,

$$\mathbf{x}_1 = A_1 \cdot \hat{\mathbf{h}}^{\text{s1}} + \mathbf{n}, \quad (10a)$$

$$\mathbf{x}_2 = A_2 \cdot \hat{\mathbf{h}}^{\text{s2}} + \mathbf{n}. \quad (10b)$$

Here, the symbol $\hat{\ } over a vector implies that the vector under consideration has a unit norm with respect to the inner product defined in Eq. (9). The signals $\hat{\mathbf{h}}^{\text{s1}}$ and $\hat{\mathbf{h}}^{\text{s2}}$, when strongly lensed, will have$

the same intrinsic parameters $\vec{\theta}^3$, along with a relative difference in Morse phase. Matched filtering of the strain data \mathbf{x}_1 and \mathbf{x}_2 yields templates $\widehat{\mathbf{h}}(\vec{\theta}_1) = \widehat{\mathbf{h}}^{t_1}$ and $\widehat{\mathbf{h}}(\vec{\theta}_2) = \widehat{\mathbf{h}}^{t_2}$ from the template bank \mathcal{B} , respectively.

We aim to construct a space \mathcal{S} orthogonal to the space containing trigger $\widehat{\mathbf{h}}^{t_1}$ corresponding to the dominant signal (i.e., the signal with greater trigger SNR in the pair) and the templates lying in its neighborhood, which is our main goal for this section. This is done to get a space approximately orthogonal to the unknown signal $\widehat{\mathbf{h}}^{s_1}$. A desirable property of this orthogonal space \mathcal{S} is that the signal $\widehat{\mathbf{h}}^{s_2}$ (which will have the same phase evolution as $\widehat{\mathbf{h}}^{s_1}$ when strongly lensed), should have a small projection onto the orthogonal space. Also, the signal $\widehat{\mathbf{h}}^{s_2}$ should project heavily onto the orthogonal space when the pair under consideration is unlensed. Now to construct \mathcal{S} , we start with the trigger template $\widehat{\mathbf{h}}^{t_1}$ and define the set of neighborhood templates $\{\widehat{\mathbf{h}}_\alpha\}$ selected from the template bank \mathcal{B} by setting a match (complex inner product maximized over time t_c and phase ϕ_c at coalescence) threshold μ (e.g., 0.97) between trigger template $\widehat{\mathbf{h}}^{t_1}$ and template $\widehat{\mathbf{h}}^t$ from the bank as follows:

$$\{\widehat{\mathbf{h}}_\alpha\} = \left\{ \widehat{\mathbf{h}}^t \in \mathcal{B} \mid \left(\widehat{\mathbf{h}}^t, \widehat{\mathbf{h}}^{t_1} \right)_{\max(t_c, \phi_c)} \geq \mu \right\}. \quad (11)$$

The index α runs from 1 to J , where J is the number of templates in $\{\widehat{\mathbf{h}}_\alpha\}$. Clearly, the trigger template $\widehat{\mathbf{h}}^{t_1}$ is included in this collection. Now, certain regions of the parameter space in the template bank might be overdense⁴ in the number of templates. If the trigger template $\widehat{\mathbf{h}}^{t_1}$ happens to lie in such a region of parameter space, we might encounter a situation where we have a large number of templates, say ~ 100 , in the neighborhood of the trigger template. This could make our computation of the χ^2 cumbersome.

In order to deal with this kind of situation, we use the Singular Value Decomposition (SVD). We construct a matrix \mathbf{M} as follows: We consider the templates $\widehat{\mathbf{h}}_\alpha$ in the frequency domain and consider only positive frequency components, with frequencies between f_{\min} and f_{\max} . Then $\widehat{\mathbf{h}}_\alpha$ can be thought of as complex vectors on the interval $[f_{\min}, f_{\max}]$. These vectors are in \mathcal{H} . Since

we are in a complex space, we must use the scalar product defined by Eq. (9) on \mathcal{H} rather than the one given by Eq. (2). We need to whiten the row vectors $\widehat{\mathbf{h}}_\alpha$ before applying the SVD. This is because the standard SVD algorithm uses the Euclidean scalar product without the PSD. This results in the matrix \mathbf{M} consisting of J row vectors, which span a J dimensional complex vector space \mathcal{W}_J , assuming the templates to be linearly independent. But since J may be large, we use the SVD to whittle down the row dimension of \mathbf{M} and get the best low dimensional approximation to \mathcal{W}_J . This approximate space we call \mathcal{V} . The SVD implementation is described in detail in Section III B. Further, the SVD also gives us an orthonormal set of vectors $\{\widehat{\mathbf{w}}_\alpha\}$ - the right singular vectors - which then form an orthonormal basis of \mathcal{W}_J . When J is large, it is usually possible to make the dimension j of \mathcal{V} much less than J . We then unwhiten the singular vectors corresponding to the most significant singular values by multiplying them with $\sqrt{S_n(f)}$ to obtain a set $\{\widehat{\mathbf{v}}_\alpha\}$ which span a space \mathcal{V} .

The next step is to obtain a space \mathcal{S} orthogonal to \mathcal{V} , which will then be at least approximately orthogonal to the linear span of the neighborhood templates, namely, the collection $\widehat{\mathbf{h}}_\alpha$. Given a template with coalescence phase equal to zero, say $\widehat{\mathbf{h}}_0$, we can obtain the template with phase $\pi/2$ by just multiplying it by i , since we are only considering positive frequencies, that is, $\widehat{h}_{\pi/2}(f) = i\widehat{h}_0(f)$ or in vector notation, $\widehat{\mathbf{h}}_{\pi/2} = i\widehat{\mathbf{h}}_0$. Both $\widehat{\mathbf{h}}_0$ and $\widehat{\mathbf{h}}_{\pi/2}$ are regarded as complex vectors. In the complex space, the two vectors are complex multiples of each other. So, we need to consider only one of them, say $\widehat{\mathbf{h}}_0$. We, therefore, proceed to construct a complex vector orthogonal to the space \mathcal{V} . We do this by subtracting out the component of $\widehat{\mathbf{h}}_0^{t_2}$ which project onto the space \mathcal{V} . Therefore, we have,

$$\begin{aligned} \Delta \mathbf{h} &= \widehat{\mathbf{h}}_0^{t_2} - \mathbf{v} \\ &= \widehat{\mathbf{h}}_0^{t_2} - \sum_{\alpha=1}^j \left(\widehat{\mathbf{v}}_\alpha, \widehat{\mathbf{h}}_0^{t_2} \right) \widehat{\mathbf{v}}_\alpha, \end{aligned} \quad (12)$$

where $\mathbf{v} = \sum_{\alpha=1}^j \left(\widehat{\mathbf{v}}_\alpha, \widehat{\mathbf{h}}_0^{t_2} \right) \widehat{\mathbf{v}}_\alpha$ is the component of $\widehat{\mathbf{h}}_0^{t_2}$ parallel to \mathcal{V} . Thus, by construction, $\Delta \mathbf{h}$ is orthogonal to \mathcal{V} , and it spans the space \mathcal{S} of one complex dimension. This corresponds to the two real dimensions of the two phases $0, \pi/2$. We note that $\Delta \mathbf{h}$ is a complex vector accommodating both phases. However, it is not normalized. The normalized vector is given by

$$\widehat{\Delta \mathbf{h}} = \frac{\Delta \mathbf{h}}{\|\Delta \mathbf{h}\|}, \quad (13)$$

where the norm is computed from the scalar product in Eq. (9). The corresponding complex correlation is

³ In this work, we consider non-spinning CBC sources that emit dominant-mode signals. For simplicity, we also neglect the effects of eccentricity and spin-orbit precession. However, the method we propose is expected to work in general as long as the images exhibit phase-evolution consistency.

⁴ This is particularly the case for the high mass region of the parameter space if one is using a geometric bank.

the projection of the data vector \mathbf{x}_2 onto $\widehat{\Delta\mathbf{h}}$, that is, $\Delta C = (\mathbf{x}_2, \widehat{\Delta\mathbf{h}})$. The χ^2 statistic is given by

$$\chi_{\text{lens}}^2 = |\Delta C|^2. \quad (14)$$

In Gaussian noise, χ_{lens}^2 has a non-central χ^2 distribution with two degrees of freedom in general (see Section III D).

B. Singular Value Decomposition

In this section, we describe the SVD and its necessity in our work. As discussed in the previous section, certain trigger templates may have a large number of templates in their corresponding neighborhood, many of which are redundant. The SVD algorithm is a powerful tool to reduce the number of vectors needed while preserving the essential characteristics of the space spanned by the neighborhood template vectors $\widehat{\mathbf{h}}_\alpha$.

To achieve this reduction, we proceed with the following steps:

- We first prepare the SVD input matrix \mathbf{M} by taking frequency domain normalised templates $\widehat{\mathbf{h}}_\alpha$, which are defined in the positive frequency range $[f_{\min}, f_{\max}]$. Since we are using the scalar product of two vectors defined in Eq. (9), which is an inner product weighted inversely by $S_n(f)$, we need to whiten the templates by dividing each of them by $\sqrt{S_n(f)}$. This is required because the SVD algorithm uses Euclidean inner product.
- The SVD input matrix \mathbf{M} is now defined as the matrix whose α th row is the complex vector $\widehat{\mathbf{h}}_\alpha(f)/\sqrt{S_n(f)}$. Thus, the resulting matrix will be $(J \times K)$ dimensional, where J and K are the number of templates and the number of frequency sample points of a vector, respectively.
- The SVD algorithm factorizes the matrix \mathbf{M} as a product of 3 matrices

$$\mathbf{M}_{(J \times K)} = \mathbf{U}_{(J \times R)} \boldsymbol{\Sigma}_{(R \times R)} \mathbf{V}_{(R \times K)}^\dagger. \quad (15)$$

Here $R \leq \min(J, K)$ is the ‘rank’ or the number of linearly independent columns/rows of the input matrix \mathbf{M} . Matrix $\boldsymbol{\Sigma}$ is a diagonal matrix, which contains the real and positive singular values (σ) sorted in descending order. Also, \mathbf{U} and \mathbf{V} are complex unitary matrices whose columns consist of the left and right singular vectors, respectively, forming an orthonormal basis for the column and row spaces of \mathbf{M} .

- Although the row vectors of \mathbf{V}^\dagger form an orthonormal basis for the row space of \mathbf{M} , many of them may be redundant on account of overdensity of templates in certain regions of the parameter space. We aim to retain only the most significant basis vectors for our analysis while preserving the essential properties of the row space of \mathbf{M} . Specifically, we seek the best low-dimensional approximation to the row space of \mathbf{M} . This is achieved by selecting the first j row vectors of \mathbf{V}^\dagger corresponding to the largest singular values. Given the Frobenius norm of the SVD input matrix is $\|\mathbf{M}\|_{\text{Frob}} = \sum_{\alpha=1}^J \sigma_\alpha^2$,

$$\sum_{\alpha=1}^j \sigma_\alpha^2 \geq \zeta \|\mathbf{M}\|_{\text{Frob}}, \quad j \leq J. \quad (16)$$

To ensure that the essential characteristics of the vector space are preserved, we set $\zeta = 99.9\%$ in our analysis.

- Finally, we unwhiten each significant basis vector by multiplying each frequency sample point of a vector by $\sqrt{S_n(f)}$. The set of vectors, $\{\widehat{\mathbf{v}}_\alpha\}$, forms an orthonormal basis with respect to the inner product defined in Eq. (9). This basis’s linear span is \mathcal{V} , which best approximates the space spanned by $\{\widehat{\mathbf{h}}_\alpha\}$.

C. χ_{lens}^2 for lensed and unlensed pairs

In this section, we investigate the distribution of χ_{lens}^2 . We find that it possesses a non-central χ^2 distribution in general. We evaluate its mean value and variance for lensed and unlensed pairs. For now, we assume that the template associated with the second signal is a perfect representation of that signal. In the following section, we will investigate the effect of a small mismatch between signal and template.

To start, it is straightforward to see that

$$\left(\widehat{\mathbf{h}}_0^{t_2}, \Delta\mathbf{h}\right) = 1 - \sum_{\alpha=1}^j |\mathcal{M}_\alpha|^2, \quad (17)$$

where

$$\mathcal{M}_\alpha \equiv \left(\widehat{\mathbf{h}}_0^{t_2}, \widehat{\mathbf{v}}_\alpha\right). \quad (18)$$

Equation (17) also gives the square of the norm of $\Delta\mathbf{h}$ because $\widehat{\mathbf{h}}_0^{t_2} = \Delta\mathbf{h} + \mathbf{v}$, for some vector $\mathbf{v} \in \mathcal{V}$ and since $(\mathbf{v}, \Delta\mathbf{h}) = 0$, the result follows. Thus,

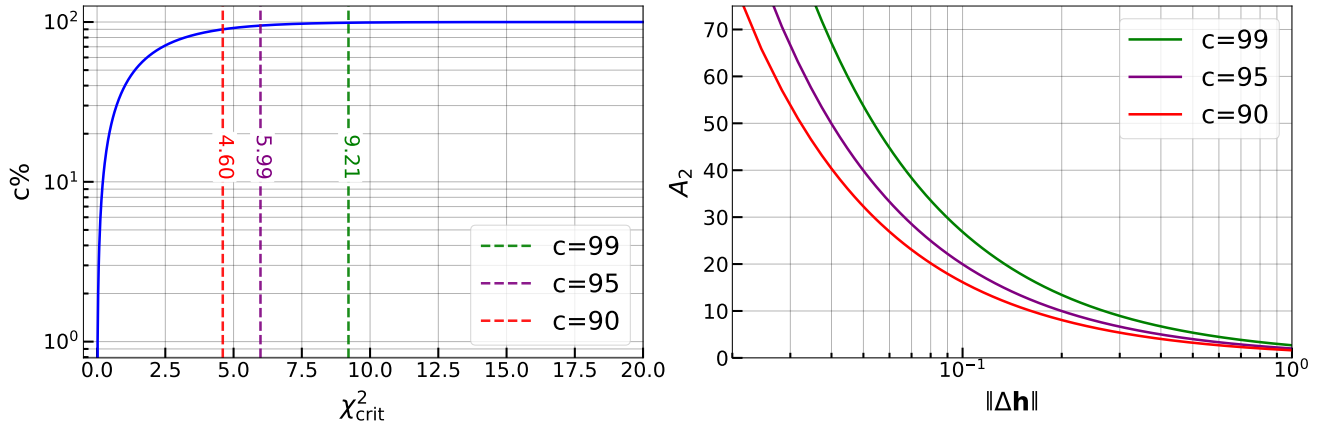


Figure 1. (Left) Confidence $c\%$ vs. χ_{crit}^2 . Any pair of events having $\chi_{\text{lens}}^2 \leq \chi_{\text{crit}}^2|_{c\%}$ could be classified as unlensed with $c\%$ confidence, assuming χ_{lens}^2 for lensed cases is a central χ^2 ($\lambda = 0$) distribution. (Right) The minimum amplitude (A_2) required to classify a truly unlensed pair as unlensed vs. $\|\Delta\mathbf{h}\|$ for varying $c\%$. Smaller projection of the template $\hat{\mathbf{h}}_0^{\text{t}_2}$ onto the orthogonal space results in $\|\Delta\mathbf{h}\|$ approaching zero, necessitating larger amplitudes for unlensed classification at the same confidence level.

$$\|\Delta\mathbf{h}\| = \sqrt{(\Delta\mathbf{h}, \Delta\mathbf{h})} = \sqrt{1 - \sum_{\alpha=1}^j |\mathcal{M}_{\alpha}|^2}, \quad (19a)$$

$$\|\mathbf{v}\| = \sqrt{(\mathbf{v}, \mathbf{v})} = \sqrt{\sum_{\alpha=1}^j |\mathcal{M}_{\alpha}|^2}. \quad (19b)$$

Assuming a perfect match between signal and template, a signal with an arbitrary phase is $\hat{\mathbf{h}}^{\text{s}_2} = \hat{\mathbf{h}}_0^{\text{t}_2} e^{i\phi}$. The absolute value of the complex correlation, in the absence of noise, is then,

$$|\Delta C| = \left| (A_2 \hat{\mathbf{h}}^{\text{s}_2}, \widehat{\Delta\mathbf{h}}) \right| = \left| e^{-i\phi} A_2 (\hat{\mathbf{h}}_0^{\text{t}_2}, \widehat{\Delta\mathbf{h}}) \right| = A_2 \|\Delta\mathbf{h}\|. \quad (20)$$

In the presence of stationary Gaussian noise, ΔC is a Gaussian random variable with mean $(A_2 \hat{\mathbf{h}}^{\text{s}_2}, \widehat{\Delta\mathbf{h}})$ and unit variance for both degrees of freedom. The correlation modulus squared then becomes a non-central χ^2 random variable, χ_{lens}^2 having two degrees of freedom⁵ with noncentrality parameter $\lambda = \left| (A_2 \hat{\mathbf{h}}^{\text{s}_2}, \widehat{\Delta\mathbf{h}}) \right|^2$. Its mean value is

$$\begin{aligned} \langle \chi_{\text{lens}}^2 \rangle &= \lambda + 2 \\ &= |A_2|^2 \|\Delta\mathbf{h}\|^2 + 2. \end{aligned} \quad (21)$$

The variance $\sigma_{\chi_{\text{lens}}^2}^2$ (not to be confused with the singular values described in Section III B) of χ_{lens}^2 is then⁶,

$$\sigma_{\chi_{\text{lens}}^2}^2 = 4(1 + \lambda). \quad (22)$$

When a pair of events are lensed, the second signal can be expressed, to a very good approximation, as a linear combination of $\hat{\mathbf{v}}_{\alpha}$. Indeed, if the second template perfectly matches one of the templates neighboring the first signal, $\hat{\mathbf{h}}_{\alpha}$, then the linear combination becomes an exact representation. In other words, the projection of the second signal onto subspace \mathcal{S} vanishes completely. It follows that, for lensed pairs, χ_{lens}^2 acquires the central χ^2 distribution with $\langle \chi_{\text{lens}}^2 \rangle = 2$ and $\sigma_{\chi_{\text{lens}}^2}^2 = 4$.

$\langle \chi_{\text{lens}}^2 \rangle$ for an unlensed pair grows as the square of the amplitude of the second signal, $|A_2|^2$. Moreover, it depends on the consistency (or lack thereof) between the two signals in the unlensed pair, quantified by $\|\Delta\mathbf{h}\|$. Chance astrophysical coincidences, which result in approximately similar source parameters for signals in the unlensed pair, will require larger SNRs to be confidently identified as unlensed. In other words, false alarms are reduced with increased signal amplitudes.

To get a better understanding of the ability of χ_{lens}^2 to discriminate between lensed and unlensed pairs, it is instructive to consider the following illustrative example. Let us suppose that we wish to correctly identify a pair of unlensed GW events at $c\%$ confidence.

⁵ χ_{lens}^2 has two degrees of freedom because ΔC is the sum of two unit-variance Gaussian random variables, one each for the real and imaginary part.

⁶ Variance of a non-central χ^2 distribution with p degrees of freedom having non-centrality parameter λ is $2(p + 2\lambda)$.

We note that the relevant distribution is the central χ^2 with 2 degrees of freedom. This is just the exponential distribution. We need the CDF of this distribution, which is

$$P(z \leq Z) = 1 - e^{-Z/2}. \quad (23)$$

Setting $Z = \chi_{\text{crit}}^2$ and $P(Z) = c/100$ we obtain,

$$\chi_{\text{crit}}^2 = 2 \ln \left[\frac{100}{100 - c} \right]. \quad (24)$$

Then, on average, dismissal of an unlensed pair at $> c\%$ confidence would translate to the following condition on the amplitude of the second signal

$$\langle \chi_{\text{lens}}^2 \rangle_{\text{UL}} > \chi_{\text{crit}}^2 \Rightarrow |A_2|^2 > \frac{\chi_{\text{crit}}^2 - 2}{\|\Delta \mathbf{h}\|}. \quad (25)$$

D. Effect of mismatch

In this section, we consider a more realistic scenario in which the second signal, $\hat{\mathbf{h}}^{s_2}$, and the corresponding trigger template, $\hat{\mathbf{h}}_0^{t_2}$, have different intrinsic parameters. If the SNR of the signal is reasonably large, the signal will generally lie in the immediate neighborhood of the trigger template (but this may not always happen). However, here we will assume that the signal lies in the immediate neighborhood, defined by the mismatch parameter ϵ , of the trigger template. Consider a template $\hat{\mathbf{h}}_{\phi}^{t_2} = \hat{\mathbf{h}}_0^{t_2} e^{i\phi}$ with $\phi = \phi_{\text{max}}$ such that the inner product $\left(\hat{\mathbf{h}}^{s_2}, \hat{\mathbf{h}}_{\phi}^{t_2} \right)_{\phi=\phi_{\text{max}}}$ is maximized. Since there is a mismatch between the signal and the template, this inner product will be less than one.

Now, the signal can be written as,

$$\hat{\mathbf{h}}^{s_2} = \hat{\mathbf{h}}_{\phi_{\text{max}}}^{t_2} + \delta \mathbf{h}. \quad (26)$$

From the previous section,

$$\begin{aligned} \left| \left(\hat{\mathbf{h}}_{\phi_{\text{max}}}^{t_2}, \widehat{\Delta \mathbf{h}} \right) \right| &= \left| e^{-i\phi_{\text{max}}} A_2 \left(\hat{\mathbf{h}}_0^{t_2}, \widehat{\Delta \mathbf{h}} \right) \right| \\ &= A_2 \|\Delta \mathbf{h}\|. \end{aligned} \quad (27)$$

Also, it has been shown in [1] that in case of mismatch between the signal and the template, the norm of $\delta \mathbf{h}$ is bounded above by

$$\|\delta \mathbf{h}\| \leq \sqrt{2\epsilon}. \quad (28)$$

Using the Cauchy-Schwartz inequality, it can be shown that the quantity $\left| \left(\delta \mathbf{h}, \widehat{\Delta \mathbf{h}} \right) \right|$ has an upper bound

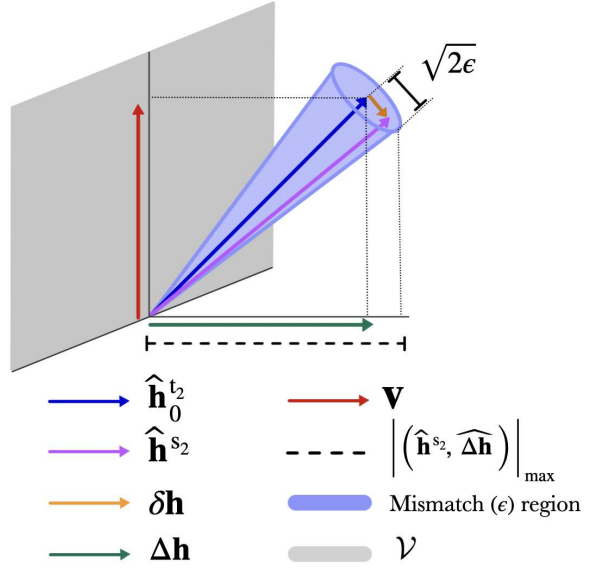


Figure 2. A visual representation of the bound presented in Eq. (30). The approximate neighborhood space \mathcal{V} has been represented by a plane (grey). The zero phase trigger template $\hat{\mathbf{h}}_0^{t_2}$ has a component \mathbf{v} (red) in the space \mathcal{V} , while the other component $\Delta \mathbf{h}$ (dark green) being orthogonal to it. We assume that the signal $\hat{\mathbf{h}}^{s_2}$ (purple) lies in the immediate neighborhood (violet cone) of the trigger template. The length of the difference vector $\delta \mathbf{h}$ (orange) is bounded above by $\sqrt{2\epsilon}$. It can also be seen that the projection of the signal onto the orthogonal space has an upper bound (dashed line).

$$\left| \left(\delta \mathbf{h}, \widehat{\Delta \mathbf{h}} \right) \right| \leq \|\delta \mathbf{h}\| \cdot \|\widehat{\Delta \mathbf{h}}\| \leq \sqrt{2\epsilon}. \quad (29)$$

Eventually, using the triangle inequality for complex numbers, it can be shown that the absolute value of the mean of correlation parameter ΔC is bounded above as,

$$\begin{aligned} |\langle \Delta C \rangle| &= \left| \left(A_2 \hat{\mathbf{h}}^{s_2}, \widehat{\Delta \mathbf{h}} \right) \right| \\ &= A_2 \left| \left(\hat{\mathbf{h}}_{\phi_{\text{max}}}^{t_2}, \widehat{\Delta \mathbf{h}} \right) + \left(\delta \mathbf{h}, \widehat{\Delta \mathbf{h}} \right) \right| \\ &\leq A_2 \left(\left| \left(\hat{\mathbf{h}}_{\phi_{\text{max}}}^{t_2}, \widehat{\Delta \mathbf{h}} \right) \right| + \left| \left(\delta \mathbf{h}, \widehat{\Delta \mathbf{h}} \right) \right| \right) \\ &\leq A_2 \left(\|\Delta \mathbf{h}\| + \sqrt{2\epsilon} \right). \end{aligned} \quad (30)$$

This bound has been illustrated in Fig 2. The mean of the χ_{lens}^2 is then

$$\langle \chi_{\text{lens}}^2 \rangle \leq (A_2)^2 \left(\|\Delta \mathbf{h}\| + \sqrt{2\epsilon} \right)^2 + 2. \quad (31)$$

We now want to highlight the importance of constructing a space orthogonal to the neighborhood space

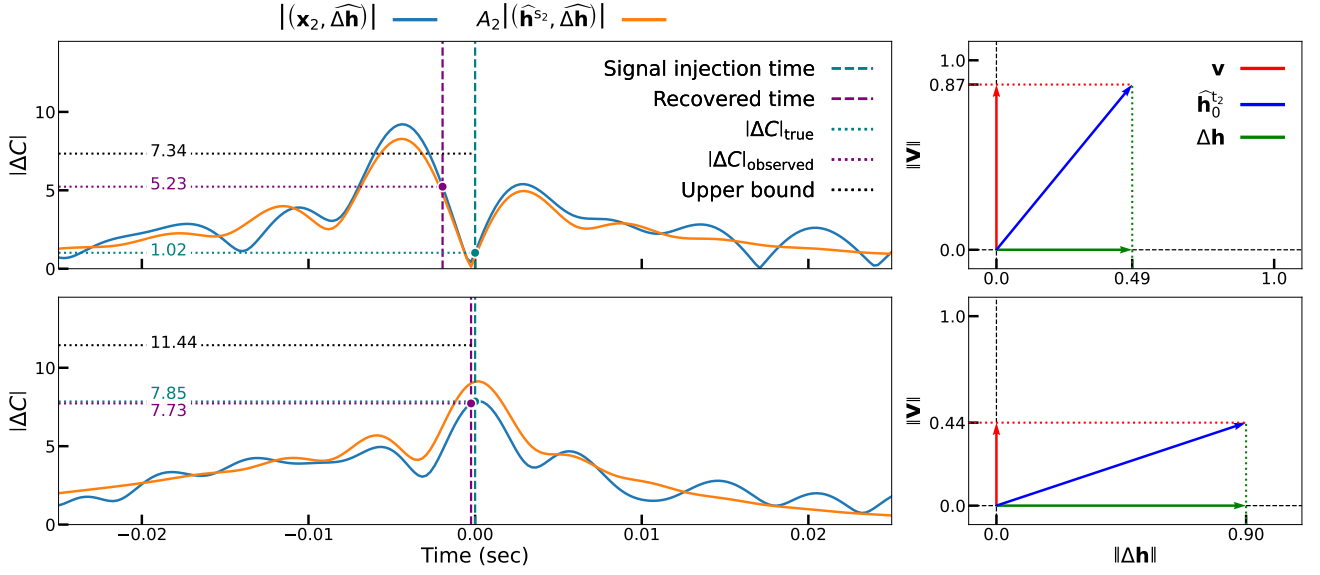


Figure 3. The $|\Delta C(t)|$ time-series for the lensed (top left) and unlensed case (bottom left) with/without noise when $\Delta \mathbf{h} \perp \widehat{\mathbf{h}}^{t_1}$. We observe a sharp dip at the merger time $t = 0$ sec for the lensed case and a peak for the unlensed case. Due to an error in locating the signal merger time from matched filtering, we end up observing $|\Delta C|_{\text{observed}}$ (purple) instead of $|\Delta C|_{\text{true}}$ (teal). It should also be noted that $|\Delta C|_{\text{true}}$ in both lensed/unlensed cases is well below the upper bound on $|\langle \Delta C \rangle|$ (black) derived in Eq. (30) for $\epsilon = 0.97$. The top/bottom right plots show the parallel (red) and perpendicular (green) components of $\widehat{\mathbf{h}}_0^{t_2}$ to the template $\widehat{\mathbf{h}}^{t_1}$ for the lensed/unlensed cases respectively. Both the trigger templates are more aligned towards each other in the lensed case compared to the unlensed case quantified by $\|\Delta \mathbf{h}\|$.

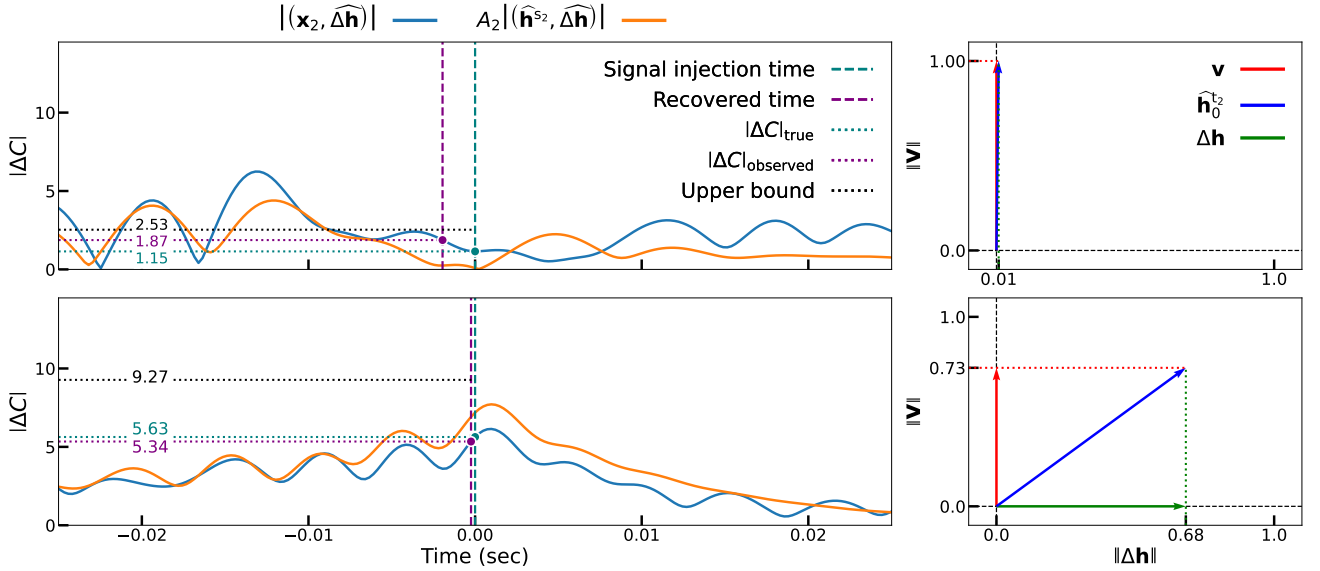


Figure 4. The $|\Delta C(t)|$ time-series for the lensed (top left) and unlensed case (bottom left) with/without noise when $\Delta \mathbf{h} \perp \mathcal{V}$. We observe a broader flattening of the correlation parameter time-series around the merger time $t = 0$ sec for the lensed case and a slight depreciation of the peak for the unlensed case compared to the single template case in Fig. 3. Again, the $|\Delta C|_{\text{true}}$ (teal) is smaller than the upper bound (black) on $|\langle \Delta C \rangle|$ for both lensed/unlensed cases. We also observe that $\widehat{\mathbf{h}}_0^{t_2}$ is almost fully contained in the space \mathcal{V} as $\|\mathbf{v}\| \approx 1$ for the lensed case (top right) making it a better discriminator compared to the single template case, although this also follows up with a relative increase in $\|\mathbf{v}\|$ for the unlensed case (bottom right) compared to the single template case in Fig. 3.

\mathcal{V} rather than only the trigger template $\hat{\mathbf{h}}_0^{t_1}$. Figures 3 and 4 show the $|\Delta C|$ time series for the lensed and unlensed cases with/without noise when:

- $\Delta \mathbf{h}$ is orthogonal to the single template $\hat{\mathbf{h}}_0^{t_1}$.
- $\Delta \mathbf{h}$ is orthogonal to the space \mathcal{V} .

Here, we show the case of a lensed event pair with signals having chirp mass (M_c) of $36.9 M_\odot$ and different amplitudes with $A_1 = 15$ and $A_2 = 10$, injected in different noise realizations. Similarly, for the unlensed case, we inject two signals with $M_c^{(1)} = 36.9 M_\odot$ and $M_c^{(2)} = 31.7 M_\odot$, having amplitudes $A_1 = 15$ and $A_2 = 10$ respectively in different noise realizations. The signals have their merger time at $t = 0$ sec.

Matched filtering of both the strain data with the templates in the template bank gives us the trigger templates with the highest trigger SNR. Figure 3 (top and bottom left for lensed and unlensed cases respectively) shows the case when $|\Delta C|$ time-series is evaluated with/without noise for the vector $\Delta \mathbf{h}$ defined as

$$\Delta \mathbf{h} = \hat{\mathbf{h}}_0^{t_2} - \left(\hat{\mathbf{h}}^{t_1}, \hat{\mathbf{h}}_0^{t_2} \right) \hat{\mathbf{h}}^{t_1}. \quad (32)$$

In the single template case, the parallel component of $\hat{\mathbf{h}}_0^{t_2}$ turns out to be $\mathbf{v} = \left(\hat{\mathbf{h}}^{t_1}, \hat{\mathbf{h}}_0^{t_2} \right) \hat{\mathbf{h}}^{t_1}$. For the lensed case, we expect a dip at $t = 0$ sec since $\Delta \mathbf{h} \perp \hat{\mathbf{h}}^{t_1}$. We indeed observe a sharp dip at $t = 0$ sec, but due to uncertainty in locating the signal merger time from matched filtering, we may end up observing $|\Delta C|$ at $t \neq 0$ instead of the true one at $t = 0$. Similarly, we also show the unlensed case, where we expect some kind of a peak at the merger location. On the right-hand side of the figure, we show the parallel (\mathbf{v}) and perpendicular ($\Delta \mathbf{h}$) components of $\hat{\mathbf{h}}_0^{t_2}$ (top and bottom for lensed and unlensed case, respectively). An efficient discriminator would have $\|\mathbf{v}\|$ close to unity for the lensed case while being as small as possible for the unlensed case.

Figure 4 (top left) is for the case when $\Delta \mathbf{h} \perp \mathcal{V}$, where we find around 15 templates within 0.97 match of $\hat{\mathbf{h}}^{t_1}$, which after SVD truncation is reduced to 5. We note that the dip around the merger time flattens out over a wider range around the signal merger time for the lensed case, hence mitigating the effect of getting a higher correlation for the lensed case due to errors in locating the merger time. Also note that $\|\mathbf{v}\| \approx 1$ implies that $\hat{\mathbf{h}}_0^{t_2}$ projects very well on to the space \mathcal{V} . Choosing a wider neighborhood with lower match criteria tends to increase the number of false alarms. For our simulations discussed in the next section, we perform our analysis with the neighborhood of $\mu = 0.97$, which turns out to be the optimal match criteria for the population model used in this analysis.

IV. RESULTS

We test the performance of χ_{lens}^2 on the DST dataset used in [53]. The DST dataset contains ~ 300 lensed injection pairs and 1000 unrelated injections, which we then combined pairwise to get around half a million unlensed pairs for our analysis, making the lensed to unlensed pairs ratio $\sim 1/1600$. The distribution of injection parameters, along with the template bank parameters, is shown in Fig. 5. The template bank used in our analysis is a 3.5 PN geometric bank [88]. Since the injection parameters do not include spins, it is useful to visualize the intrinsic parameters in *chirp time* (τ) coordinates defined as follows,

$$\tau_0 = \frac{5}{256\pi\eta f_{\text{low}}} (\pi M_{\text{tot}} f_{\text{low}})^{-5/3}, \quad (33a)$$

$$\tau_3 = \frac{1}{8\eta f_{\text{low}}} (\pi M_{\text{tot}} f_{\text{low}})^{-2/3}. \quad (33b)$$

Here τ_0 is the Newtonian time of coalescence of the signal, and τ_3 corresponds to the 1.5 PN order. Also, η is the ratio of the reduced mass to the total mass M_{tot} . For all the computations, we use the zero-detuned high-power PSD of Advanced LIGO at design sensitivity, with lower frequency cutoff $f_{\text{low}} = 15$ Hz, as implemented in PyCBC [89]. All waveforms for both the signal and templates are generated using the IMRPHENOMD waveform approximant [90, 91]. Since χ_{lens}^2 is a single detector test, we *rescale the luminosity distances* for all the injections so that the signal amplitude ($A_{1,2}$) is at least 8.

We assess the performance of χ_{lens}^2 discriminator by comparing its receiver operator characteristic (ROC) curve with that of the posterior overlap statistic B_U^L [73], which uses the posteriors of the component masses (m_1, m_2). A ROC for the single detector machine learning classifier [75] is also shown. The ROC comparison, along with a histogram of χ_{lens}^2 statistic evaluated for each of the lensed/unlensed event pairs, has been shown in Fig. 6. We find that the performance of χ_{lens}^2 is comparable to the B_U^L statistic, quantified by Area Under the Curve (AUC) of the ROC, which for χ_{lens}^2 (AUC=0.93) is marginally larger than B_U^L (AUC=0.91) and non-trivially larger than the single detector machine learning classifier (AUC=0.81).

We further test the performance of χ_{lens}^2 statistic across various τ_0 bins for varying SNR combinations. We define a parameter space region with $m_1, m_2 \in [5.5M_\odot, 140M_\odot]$ and the mass ratio $q \leq 5$ ⁷, which in τ coordinates has been shown in Fig. 7.

⁷ $q \equiv m_1/m_2, m_1 \geq m_2$.

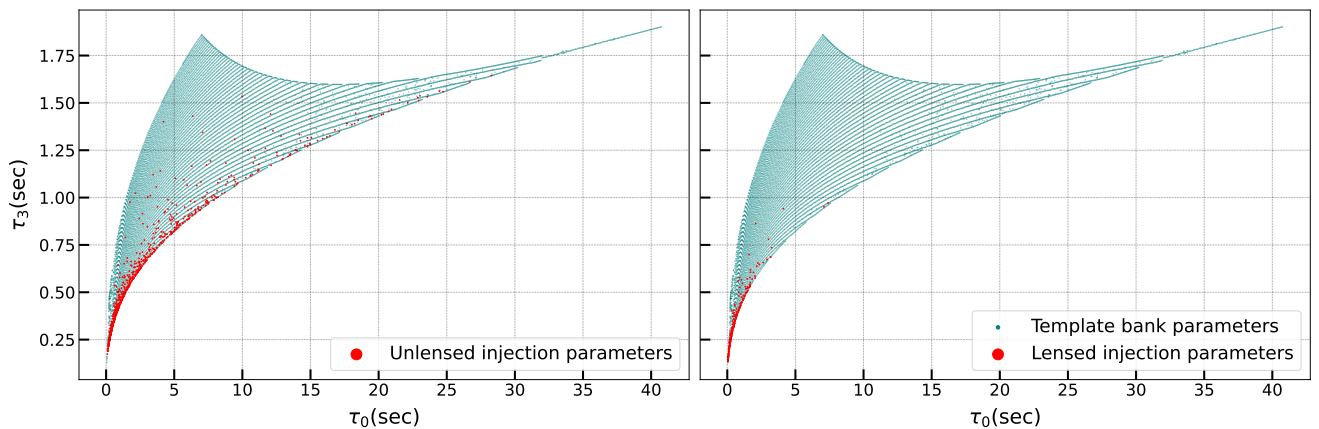


Figure 5. Chirp-time coordinates (τ_0 and τ_3) of unlensed injections (left) and lensed injections (right) taken from the DST data set used in [53]. The same coordinates pertaining to the templates in the bank are also plotted.

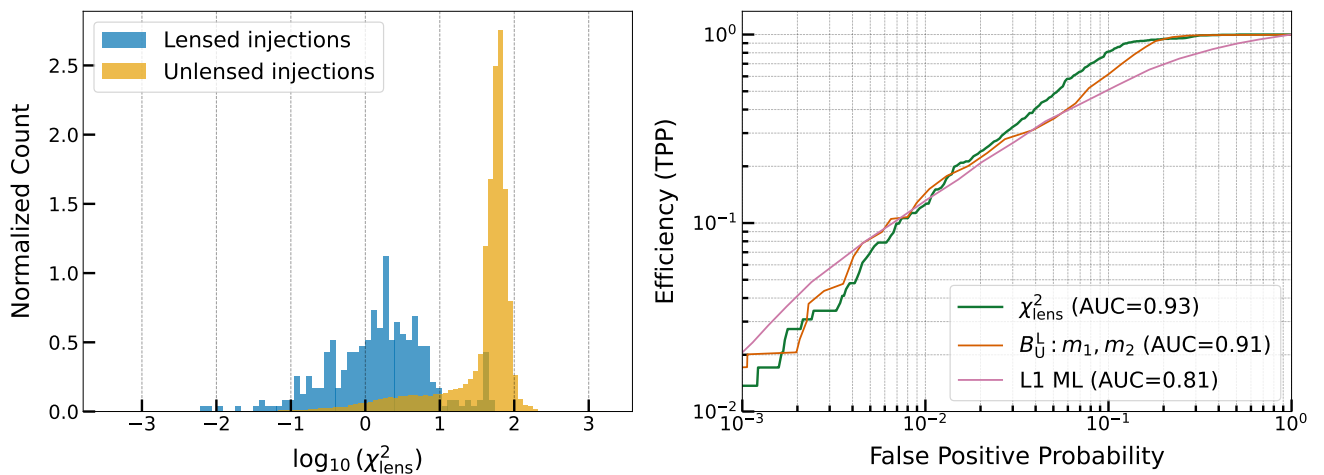


Figure 6. (Left) The histograms of $\log_{10}(\chi_{\text{lens}}^2)$ computed for lensed and un-lensed signals in the DST dataset. (Right) ROC curves for χ_{lens}^2 statistic tested on DST dataset (green), the $m_1, m_2 B_U^L$ statistic (orange) from [73] and single detector machine learning classifier (pink) from [75]. The figure shows that the performance of χ_{lens}^2 (AUC = 0.93) is comparable to that of $m_1, m_2 B_U^L$ (AUC = 0.91), while it is significantly better than single detector machine learning (ML) classifier (AUC = 0.81).

We divide the whole region into three equal areas and draw 300 and 1000 uniform samples of $\tau_0 - \tau_3$ parameters for the lensed and unlensed analysis, respectively, from each τ_0 bin. In each bin, we test the performance of χ_{lens}^2 by rescaling the luminosity distance so that the amplitudes (A_1, A_2) for signals in the event pair are (8, 7), (12, 9) and (15, 12). Figure 8 shows the ROC curves for each SNR combination across different τ_0 bins. We observe a consistent trend where the performance of the χ_{lens}^2 classifier, quantified by the AUC, improves as the signal duration (τ_0) increases. Also, the performance gets better with the increase in the SNRs of both signals.

V. SUMMARY AND OUTLOOK

A number of methods to search for signatures of gravitational lensing have been developed and deployed on LVK data (see, e.g., Ref. [70], and references therein). To date, no confirmed detection of GW lensing has been reported. Nevertheless, the expectation is that 0.1% – 1% of GWs detectable by the LVK detector network will be lensed [71, 72]. Thus, the first detection of strongly lensed GWs by galaxy or cluster scale lenses is anticipated to happen before the end of O5.

Our work proposes a novel χ^2 statistic to identify strongly lensed GW pairs and dismiss unlensed pairs. The method exploits the expected phase evolution con-

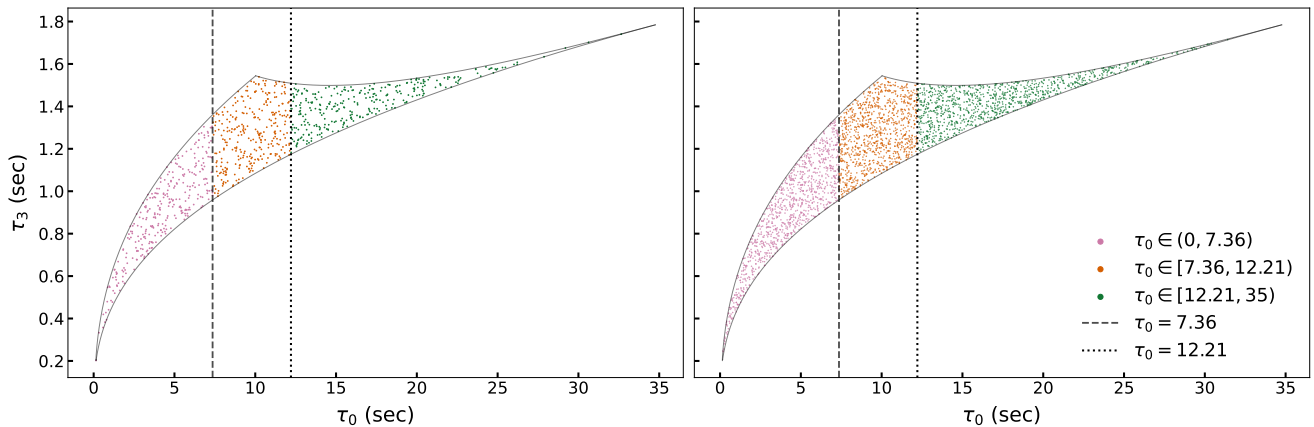


Figure 7. Chirp-time coordinates of lensed and unlensed injections for testing the performance of χ_{lens}^2 across three different τ_0 bins. Each τ_0 bin contains 300 points for lensed (left) and 1000 points for the unlensed (right) injections sampled from a uniform distribution.

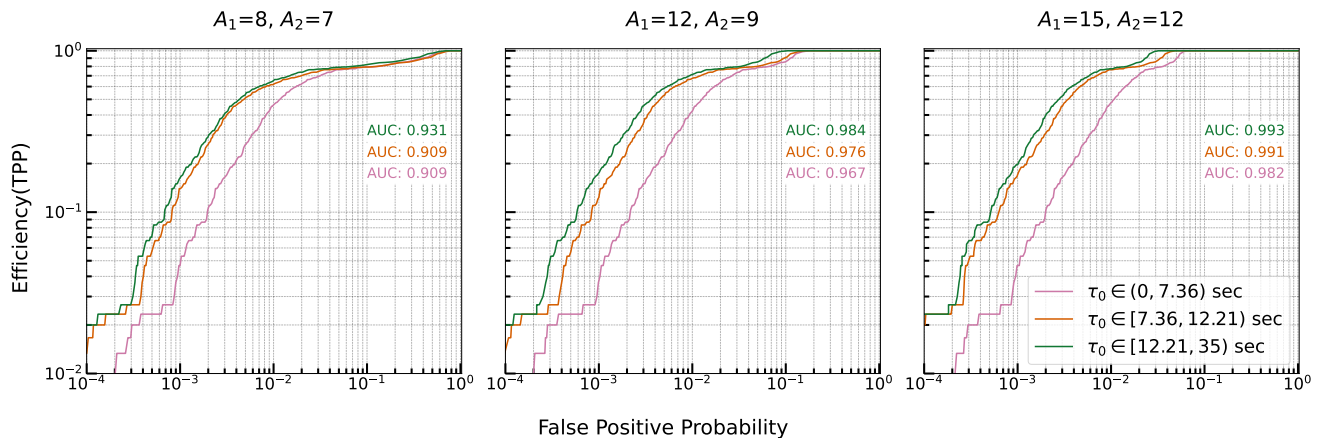


Figure 8. ROC curves for the χ_{lens}^2 statistic tested for performance across different rescaled optimal SNR combinations for the signals when (A_1, A_2) are (8, 7) (left), (12, 9) (middle) and (15, 12) (right), which are further tested across different τ_0 bins. As a measure of the performance of χ_{lens}^2 for different SNR combinations and τ_0 bins, we report AUC for each ROC curve. We find a consistent pattern that increasing the SNR of the pair for a given τ_0 bin tends to improve the ROC indicated by an increase in AUC. Also, for a given SNR combination of the pair, signals in high τ_0 bins tend to perform better due to an increase in the duration of the signals.

sistency between the events in the lensed pair, which, for unlensed pairs, should be absent. In particular, it tailors the unified χ^2 statistic delineated in Dhurandhar *et al.* [1] to the problem at hand. Using the template of the louder signal and its immediate neighborhood in the template bank, a vector orthogonal to the space spanned by said template and its neighborhood is constructed. The data pertaining to the second signal is then projected onto the orthogonal vector to construct the χ_{lens}^2 statistic.

We assess the performance of χ_{lens}^2 on a realistic astrophysical data set consisting of lensed and unlensed pairs. We find that our method provides detection efficiencies, at low false positive probabilities, that are

comparable to other standard lensing searches involving Bayesian and machine learning methods. We also find that χ_{lens}^2 systematically improves its ability to segregate lensed pairs from unlensed ones with increasing SNR and in-band signal duration. We ascertain that, indeed, the use of neighborhood around the template of the louder signal, in addition to the template itself, significantly improves the performance of χ_{lens}^2 with respect to when only the template itself is used. This fact was conjectured, in the context of the unified χ^2 , in Dhurandhar *et al.* [1], and has now been exemplified in this work.

Our method has two advantages over standard lensing searches. The first is speed. This statistic can be

evaluated in a fraction of a second per candidate pair and is readily implementable in a matched filter search pipeline. This not only allows for low-latency dissemination of GW lensing information but also significantly alleviates the computational burden required by large-scale Bayesian methods [61, 81, 83]. Moreover, χ_{lens}^2 provides a suitable alternative for the rapid (preliminary) identification of subthreshold image counterparts to superthreshold GW events [77]. Interesting candidate pairs unearthed with χ_{lens}^2 can then be further followed up with large-scale Bayesian methods. Indeed, we expect that χ_{lens}^2 can be a valuable and easily integrable addition to subthreshold search pipelines such as TESLA [92, 93].

The second is interpretation. Arguably, unlike the majority of the lensing search methods currently available, the statistics of χ_{lens}^2 are fully understood. In stationary Gaussian noise, χ_{lens}^2 for lensed pairs follow a central χ^2 distribution, while unlensed pairs follow a non-central χ^2 distribution whose mean is proportional to the squared SNR of the second (weaker) signal. This, perhaps, is the most attractive feature of χ_{lens}^2 .

It is worth reiterating that our method essentially probes phase evolution consistency between pairs of GW events. Lensing in the geometric optics regime is expected to exhibit phase evolution consistency between the images in general. However, there are exceptions where the images violate this consistency. For example, it has been shown that Type II images of GW sources with significant higher-mode content will have a phase morphology that is distinct from that of the GWs produced by the source [94–97]. On the other hand, Type I and III images will have morphologies identical to that of the source. Consequently, phase-evolution consistency between pairs of images, where exactly one of them is a Type II image of a GW source with significant higher-mode content, will be violated. Thus, all methods that look for phase-evolution consistency between GW event pairs, including ours, the traditional posterior overlap statistic method [73, 74, 77], machine learning methods [75, 76], and cross-correlation methods [79], will not work for said exceptions, without adequate modifications.

We point out that in addition to phase-evolution consistency, there are other features pertaining to strong lensing that could boost a method’s ability to identify lensed pairs. Given that the number of GW pairs grows quadratically with the number of GW events, chance astrophysical coincidences increase non-trivially with increased detector sensitivity [98]. This makes the need for additional features to help dismiss unlensed pairs all the more imperative. To that end, the expected superposition of GW localization sky areas for lensed pairs, as opposed to unlensed pairs that, is used in tandem with phase-evolution consistency by several methods. Indeed, machine learning methods construct

a separate statistic from pairs of localization sky areas and combine it with the statistic constructed from phase evolution consistency [75]. A similar approach could be adopted with χ_{lens}^2 . Furthermore, prior information involving expected image time delay and magnification distributions for galaxy and cluster scale lenses can also be used to boost the performance of a statistic. We expect that incorporating such information into our method along the lines pursued in [73, 99], should also be straightforward. We leave this for future work.

ACKNOWLEDGEMENTS

We thank Bhooshan Gadre for their reading of the manuscript. We also thank Shreejit Jadhav and Anirban Kopty for useful discussions. SG’s research was supported by the University Grants Commission, Government of India. SJK gratefully acknowledges support from the Science and Engineering Research Board (SERB) Grant SRG/2023/000419. KS acknowledges support from the National Science Foundation grant (PHY-2309240). All calculations and simulations were performed on the Sarathi computing cluster at IUCAA.

Software: PyCBC [89], NumPy [100], SciPy [101], astropy [102, 103], Matplotlib [104], jupyter [105].

Appendix A: Derivations

The Hilbert space we are dealing with is $L^2[f_{\min}, f_{\max}]$ with the weighted measure $d\mu = df/S_h(f)$, which we have already denoted by \mathcal{H} . Given time series data that is discretely sampled, we have, say, M number of frequency bins in the frequency range $[f_{\min}, f_{\max}]$. Then, the Hilbert space is just C^M with a weighted measure μ as defined. This is consistent with the practice of using a one-sided PSD with only positive frequencies.

Two different scalar products have been defined by Eqs. (2) and (9), namely, $(\mathbf{x}|\mathbf{y})$ and (\mathbf{x}, \mathbf{y}) for two vectors \mathbf{x} and \mathbf{y} on the vector space. We may easily verify that these two scalar products are related by

$$(\mathbf{x}|\mathbf{y}) = \frac{1}{2}[(\mathbf{x}, \mathbf{y}) + (\mathbf{x}, \mathbf{y})^*], \quad (\text{A1})$$

$$(\mathbf{x}, \mathbf{y}) = (\mathbf{x}|\mathbf{y}) - i(\mathbf{x}, i\mathbf{y}). \quad (\text{A2})$$

Thus, both scalar products are contentwise equivalent. So, from the mathematical point of view, we are dealing with two Hilbert spaces with their own scalar product, the vector space being the same. Eqs. (A1) and (A2) show that the two Hilbert spaces are isomorphic. Also we notice from Eq. (A1) that,

$$\|\mathbf{x}\|_{\|\cdot\|}^2 = (\mathbf{x}|\mathbf{x}) = (\mathbf{x}, \mathbf{x}) = \|\mathbf{x}\|^2, \quad (\text{A3})$$

that is, both scalar products yield the same norm for any vector $\mathbf{x} \in \mathcal{H}$.

Secondly, we note that, since we are considering complex vectors, they contain full information about the negative frequency components of the signal and also the phase information. Thus, we write a signal with coalescence phase zero as $\tilde{h}_0(f) = u(f) + iv(f)$, where $f > 0$, and $u(f), v(f)$ real. Then the following relations

hold:

$$\tilde{h}_0(-f) = \tilde{h}_0^*(f) = u(f) - iv(f), \quad (\text{A4})$$

$$\tilde{h}_{\pi/2}(f) = i\tilde{h}_0(f) = iu(f) - v(f), \quad (\text{A5})$$

$$\tilde{h}_{\pi/2}(-f) = \tilde{h}_{\pi/2}^*(f) = -iu(f) - v(f). \quad (\text{A6})$$

The above relations show that given $\tilde{h}_0(f)$ as a complex vector for $f > 0$, we can obtain the time domain signal $h_0(t)$ as well as $h_{\pi/2}(t)$ pertaining to the two coalescence phases 0 and $\pi/2$.

-
- [1] S. Dhurandhar, A. Gupta, B. Gadre, and S. Bose, *Phys. Rev. D* **96**, 103018 (2017).
- [2] J. Aasi *et al.* (LIGO Scientific), *Class. Quant. Grav.* **32**, 074001 (2015), arXiv:1411.4547 [gr-qc].
- [3] F. Acernese *et al.* (Virgo), *Class. Quant. Grav.* **32**, 024001 (2015), arXiv:1408.3978 [gr-qc].
- [4] R. Abbott *et al.* (KAGRA, VIRGO, LIGO Scientific), *Phys. Rev. X* **13**, 041039 (2023), arXiv:2111.03606 [gr-qc].
- [5] A. H. Nitz, C. D. Capano, S. Kumar, Y.-F. Wang, S. Kastha, M. Schäfer, R. Dhurkunde, and M. Cabero, *The Astrophysical Journal* **922**, 76 (2021).
- [6] S. Olsen, T. Venumadhav, J. Mushkin, J. Roulet, B. Zackay, and M. Zaldarriaga, *Phys. Rev. D* **106**, 043009 (2022).
- [7] A. H. Nitz, S. Kumar, Y.-F. Wang, S. Kastha, S. Wu, M. Schäfer, R. Dhurkunde, and C. D. Capano, *The Astrophysical Journal* **946**, 59 (2023).
- [8] A. K. Mehta, S. Olsen, D. Wadekar, J. Roulet, T. Venumadhav, J. Mushkin, B. Zackay, and M. Zaldarriaga, “New binary black hole mergers in the ligo-virgo o3b data,” (2024), arXiv:2311.06061 [gr-qc].
- [9] D. Wadekar, J. Roulet, T. Venumadhav, A. K. Mehta, B. Zackay, J. Mushkin, S. Olsen, and M. Zaldarriaga, “New black hole mergers in the ligo-virgo o3 data from a gravitational wave search including higher-order harmonics,” (2023), arXiv:2312.06631 [gr-qc].
- [10] M. Vallisneri, J. Kanner, R. Williams, A. Weinstein, and B. Stephens, *Journal of Physics: Conference Series* **610**, 012021 (2015).
- [11] R. Abbott *et al.* (LIGO Scientific, Virgo), *SoftwareX* **13**, 100658 (2021), arXiv:1912.11716 [gr-qc].
- [12] B. P. Abbott *et al.* (LIGO Scientific, Virgo), *Phys. Rev. Lett.* **119**, 161101 (2017), arXiv:1710.05832 [gr-qc].
- [13] B. Abbott *et al.* (LIGO Scientific, Virgo), *Astrophys. J. Lett.* **892**, L3 (2020), arXiv:2001.01761 [astro-ph.HE].
- [14] R. Abbott *et al.* (LIGO Scientific, KAGRA, VIRGO), *Astrophys. J. Lett.* **915**, L5 (2021), arXiv:2106.15163 [astro-ph.HE].
- [15] R. Abbott *et al.* (LIGO Scientific, VIRGO, KAGRA), (2021), arXiv:2112.06861 [gr-qc].
- [16] B. P. Abbott *et al.* (LIGO Scientific, Virgo), *Phys. Rev. Lett.* **116**, 221101 (2016), [Erratum: *Phys. Rev. Lett.* **121**, 129902 (2018)], arXiv:1602.03841 [gr-qc].
- [17] B. P. Abbott *et al.* (LIGO Scientific, Virgo), *Phys. Rev. D* **100**, 104036 (2019), arXiv:1903.04467 [gr-qc].
- [18] R. Abbott *et al.* (LIGO Scientific, Virgo), *Astrophys. J. Lett.* **900**, L13 (2020), arXiv:2009.01190 [astro-ph.HE].
- [19] A. Ghosh *et al.*, *Phys. Rev. D* **94**, 021101 (2016), arXiv:1602.02453 [gr-qc].
- [20] A. Ghosh, N. K. Johnson-Mcdaniel, A. Ghosh, C. K. Mishra, P. Ajith, W. Del Pozzo, C. P. L. Berry, A. B. Nielsen, and L. London, *Class. Quant. Grav.* **35**, 014002 (2018), arXiv:1704.06784 [gr-qc].
- [21] L. Blanchet and B. S. Sathyaprakash, *Phys. Rev. Lett.* **74**, 1067 (1995).
- [22] L. Blanchet and B. S. Sathyaprakash, *Classical and Quantum Gravity* **11**, 2807 (1994).
- [23] K. G. Arun, B. R. Iyer, M. S. S. Qusailah, and B. S. Sathyaprakash, *Phys. Rev. D* **74**, 024006 (2006), arXiv:gr-qc/0604067.
- [24] K. G. Arun, B. R. Iyer, M. S. S. Qusailah, and B. S. Sathyaprakash, *Class. Quant. Grav.* **23**, L37 (2006), arXiv:gr-qc/0604018.
- [25] N. Yunes and F. Pretorius, *Phys. Rev. D* **80**, 122003 (2009), arXiv:0909.3328 [gr-qc].
- [26] C. K. Mishra, K. G. Arun, B. R. Iyer, and B. S. Sathyaprakash, *Phys. Rev. D* **82**, 064010 (2010), arXiv:1005.0304 [gr-qc].
- [27] T. G. F. Li, W. Del Pozzo, S. Vitale, C. Van Den Broeck, M. Agathos, J. Veitch, K. Grover, T. Sidery, R. Sturani, and A. Vecchio, *Phys. Rev. D* **85**, 082003 (2012), arXiv:1110.0530 [gr-qc].
- [28] T. G. F. Li, W. Del Pozzo, S. Vitale, C. Van Den Broeck, M. Agathos, J. Veitch, K. Grover, T. Sidery, R. Sturani, and A. Vecchio, *J. Phys. Conf. Ser.* **363**, 012028 (2012), arXiv:1111.5274 [gr-qc].
- [29] B. P. Abbott *et al.* (LIGO Scientific, Virgo), *Phys. Rev. Lett.* **123**, 011102 (2019), arXiv:1811.00364 [gr-qc].
- [30] C. M. Will, *Phys. Rev. D* **57**, 2061 (1998), arXiv:gr-qc/9709011.
- [31] K. K. Y. Ng, K. W. K. Wong, T. Broadhurst, and T. G. F. Li, *Phys. Rev. D* **97**, 023012 (2018).
- [32] S.-S. Li, S. Mao, Y. Zhao, and Y. Lu, *Monthly Notices of the Royal Astronomical Society* **476**, 2220 (2018).

- [33] M. Oguri, Monthly Notices of the Royal Astronomical Society **480**, 3842 (2018).
- [34] G. P. Smith, M. Jauzac, J. Veitch, W. M. Farr, R. Massey, and J. Richard, Monthly Notices of the Royal Astronomical Society **475**, 3823 (2018).
- [35] R. J. Smith, G. Ashton, A. Vajpeyi, and C. Talbot, Monthly Notices of the Royal Astronomical Society **498**, 4492 (2020).
- [36] G. P. Smith, A. Robertson, M. Bianconi, and M. Jauzac (LSST), (2019), [arXiv:1902.05140 \[astro-ph.HE\]](#).
- [37] A. Robertson, G. P. Smith, R. Massey, V. Eke, M. Jauzac, M. Bianconi, and D. Ryczanowski, Monthly Notices of the Royal Astronomical Society **495**, 3727 (2020).
- [38] D. Ryczanowski, G. P. Smith, M. Bianconi, R. Massey, A. Robertson, and M. Jauzac, Monthly Notices of the Royal Astronomical Society **495**, 1666 (2020).
- [39] Y. Wang, A. Stebbins, and E. L. Turner, *Phys. Rev. Lett.* **77**, 2875 (1996).
- [40] L. Dai and T. Venumadhav, (2017), [arXiv:1702.04724 \[gr-qc\]](#).
- [41] J. M. Ezquiaga, D. E. Holz, W. Hu, M. Lagos, and R. M. Wald, *Phys. Rev. D* **103**, 064047 (2021).
- [42] S. Deguchi and W. D. Watson, *Phys. Rev. D* **34**, 1708 (1986).
- [43] T. T. Nakamura, *Phys. Rev. Lett.* **80**, 1138 (1998).
- [44] R. Takahashi and T. Nakamura, The Astrophysical Journal **595**, 1039 (2003).
- [45] Z. Cao, L.-F. Li, and Y. Wang, *Phys. Rev. D* **90**, 062003 (2014).
- [46] K.-H. Lai, O. A. Hannuksela, A. Herrera-Martín, J. M. Diego, T. Broadhurst, and T. G. F. Li, *Phys. Rev. D* **98**, 083005 (2018).
- [47] P. Christian, S. Vitale, and A. Loeb, *Phys. Rev. D* **98**, 103022 (2018).
- [48] L. Dai, S.-S. Li, B. Zackay, S. Mao, and Y. Lu, *Phys. Rev. D* **98**, 104029 (2018).
- [49] J. M. Diego, *Phys. Rev. D* **101**, 123512 (2020).
- [50] T. Baker and M. Trodden, *Phys. Rev. D* **95**, 063512 (2017).
- [51] T. E. Collett and D. Bacon, *Phys. Rev. Lett.* **118**, 091101 (2017).
- [52] X.-L. Fan, K. Liao, M. Biesiada, A. Piórkowska-Kurpas, and Z.-H. Zhu, *Phys. Rev. Lett.* **118**, 091102 (2017).
- [53] S. Goyal, K. Haris, A. K. Mehta, and P. Ajith, *Phys. Rev. D* **103**, 024038 (2021).
- [54] J. M. Ezquiaga and M. Zumalacárregui, *Phys. Rev. D* **102**, 124048 (2020).
- [55] M. Sereno, P. Jetzer, A. Sesana, and M. Volonteri, Monthly Notices of the Royal Astronomical Society **415**, 2773 (2011).
- [56] K. Liao, X.-L. Fan, X. Ding, M. Biesiada, and Z.-H. Zhu, *Nature Communications* **8**, 1148 (2017).
- [57] S. Cao, J. Qi, Z. Cao, M. Biesiada, J. Li, Y. Pan, and Z.-H. Zhu, *Scientific Reports* **9**, 11608 (2019).
- [58] Y. Li, X. Fan, and L. Gou, The Astrophysical Journal **873**, 37 (2019).
- [59] O. A. Hannuksela, T. E. Collett, M. Çalıřkan, and T. G. Li, Monthly Notices of the Royal Astronomical Society **498**, 3395 (2020).
- [60] S. Jana, S. J. Kapadia, T. Venumadhav, and P. Ajith, *Phys. Rev. Lett.* **130**, 261401 (2023).
- [61] S. Jana, S. J. Kapadia, T. Venumadhav, S. More, and P. Ajith, (2024), [arXiv:2408.05290 \[astro-ph.CO\]](#).
- [62] S. Magare, S. J. Kapadia, A. More, M. K. Singh, P. Ajith, and A. N. Ramprakash, *Astrophys. J. Lett.* **955**, L31 (2023), [arXiv:2302.02916 \[astro-ph.HE\]](#).
- [63] S. Basak, A. Ganguly, K. Haris, S. Kapadia, A. K. Mehta, and P. Ajith, *Astrophys. J.* **926**, L28 (2022), [arXiv:2109.06456 \[gr-qc\]](#).
- [64] A. Barsode, S. J. Kapadia, and P. Ajith, (2024), [arXiv:2405.15878 \[gr-qc\]](#).
- [65] S. Jana, S. J. Kapadia, T. Venumadhav, S. More, and P. Ajith, (2024), [arXiv:2405.17805 \[gr-qc\]](#).
- [66] U. Deka, S. Chakraborty, S. J. Kapadia, M. A. Shaikh, and P. Ajith, (2024), [arXiv:2401.06553 \[gr-qc\]](#).
- [67] S. Basak, A. K. Sharma, S. J. Kapadia, and P. Ajith, *Astrophys. J. Lett.* **942**, L31 (2023), [arXiv:2205.00022 \[gr-qc\]](#).
- [68] O. A. Hannuksela, K. Haris, K. K. Y. Ng, S. Kumar, A. K. Mehta, D. Keitel, T. G. F. Li, and P. Ajith, *Astrophys. J. Lett.* **874**, L2 (2019), [arXiv:1901.02674 \[gr-qc\]](#).
- [69] R. Abbott *et al.* (LIGO Scientific, VIRGO), *Astrophys. J.* **923**, 14 (2021), [arXiv:2105.06384 \[gr-qc\]](#).
- [70] R. Abbott *et al.* (LIGO Scientific, KAGRA, VIRGO), *Astrophys. J.* **970**, 191 (2024), [arXiv:2304.08393 \[gr-qc\]](#).
- [71] A. R. A. Wierda, E. Wempe, O. A. Hannuksela, L. V. Koopmans, and C. Van Den Broeck, The Astrophysical Journal **921**, 154 (2021).
- [72] F. Xu, J. M. Ezquiaga, and D. E. Holz, *Astrophys. J.* **929**, 9 (2022), [arXiv:2105.14390 \[astro-ph.CO\]](#).
- [73] K. Haris, A. K. Mehta, S. Kumar, T. Venumadhav, and P. Ajith, (2018), [arXiv:1807.07062 \[gr-qc\]](#).
- [74] A. Barsode, S. Goyal, and P. Ajith, (2024), [arXiv:2412.01278 \[gr-qc\]](#).
- [75] S. Goyal, H. D., S. J. Kapadia, and P. Ajith, *Phys. Rev. D* **104**, 124057 (2021), [arXiv:2106.12466 \[gr-qc\]](#).
- [76] S. Magare, A. More, and S. Choudary, (2024), [arXiv:2403.02994 \[astro-ph.HE\]](#).
- [77] S. Goyal, S. J. Kapadia, J.-R. Cudell, A. K. Y. Li, and J. C. L. Chan, *Phys. Rev. D* **109**, 023028 (2024), [arXiv:2306.04397 \[gr-qc\]](#).
- [78] J. M. Ezquiaga, W. Hu, and R. K. L. Lo, *Phys. Rev. D* **108**, 103520 (2023), [arXiv:2308.06616 \[astro-ph.CO\]](#).
- [79] A. Chakraborty and S. Mukherjee, *Mon. Not. Roy. Astron. Soc.* **532**, 4842 (2024), [arXiv:2403.03982 \[gr-qc\]](#).
- [80] X. Liu, I. M. Hernandez, and J. Creighton, The Astrophysical Journal **908**, 97 (2021).
- [81] J. Janquart, O. A. Hannuksela, K. Haris, and C. Van den Broeck, in *56th Rencontres de Moriond on Gravitation* (2022) [arXiv:2203.06444 \[gr-qc\]](#).
- [82] J. Janquart, K. Haris, O. A. Hannuksela, and C. Van Den Broeck, *Mon. Not. Roy. Astron. Soc.* **526**, 3088 (2023), [arXiv:2304.12148 \[gr-qc\]](#).
- [83] R. K. L. Lo and I. Magaña Hernandez, *Phys. Rev. D* **107**, 123015 (2023).
- [84] A. Barsode, S. Goyal, and P. Ajith, [arXiv e-prints](#),

- arXiv:2412.01278 (2024), arXiv:2412.01278 [gr-qc].
- [85] P. Joshi, R. Dhurkunde, S. Dhurandhar, and S. Bose, *Phys. Rev. D* **103**, 044035 (2021), arXiv:2006.12901 [gr-qc].
- [86] J. D. E. Creighton and W. G. Anderson, *Gravitational-wave physics and astronomy: An introduction to theory, experiment and data analysis* (John Wiley & Sons, Ltd, 2011).
- [87] B. Allen, *Phys. Rev. D* **71**, 062001 (2005), arXiv:gr-qc/0405045 [gr-qc].
- [88] S. Babak, R. Balasubramanian, D. Churches, T. Coke-laer, and B. S. Sathyaprakash, *Classical and Quantum Gravity* **23**, 5477 (2006).
- [89] A. Nitz, I. Harry, D. Brown, C. M. Biwer, J. Willis, T. D. Canton, C. Capano, T. Dent, L. Pekowsky, A. R. Williamson, S. De, M. Cabero, B. Machenschalk, D. Macleod, P. Kumar, S. Reyes, F. Pannarale, G. S. C. Davies, dfinstad, S. Kumar, M. Tápai, L. Singer, S. Khan, S. Fairhurst, A. Nielsen, S. Singh, T. Massinger, K. Chandra, Shasvath, and Veronica-villa, “gwastro/pycbc: v2.0.4 release of pycbc,” (2022).
- [90] S. Husa, S. Khan, M. Hannam, M. Pürrer, F. Ohme, X. J. Forteza, and A. Bohé, *Physical Review D* **93**, 044006 (2016).
- [91] S. Khan, S. Husa, M. Hannam, F. Ohme, M. Pürrer, X. J. Forteza, and A. Bohé, *Physical Review D* **93**, 044007 (2016).
- [92] A. K. Y. Li, R. K. L. Lo, S. Sachdev, J. C. L. Chan, E. T. Lin, T. G. F. Li, and A. J. Weinstein (LIGO Scientific, Virgo), *Phys. Rev. D* **107**, 123014 (2023), arXiv:1904.06020 [gr-qc].
- [93] A. K. Y. Li, J. C. L. Chan, H. Fong, A. H. Y. Chong, A. J. Weinstein, and J. M. Ezquiaga, (2023), arXiv:2311.06416 [gr-qc].
- [94] Y. Wang, R. K. Lo, A. K. Li, and Y. Chen, *Physical Review D* **103**, 104055 (2021).
- [95] J. Janquart, E. Seo, O. A. Hannuksela, T. G. Li, and C. Van Den Broeck, *The Astrophysical Journal Letters* **923**, L1 (2021).
- [96] A. Vijaykumar, A. K. Mehta, and A. Ganguly, *Phys. Rev. D* **108**, 043036 (2023), arXiv:2202.06334 [gr-qc].
- [97] K. Taylor, D. Davis, and R. K. L. Lo, (2024), arXiv:2412.15148 [gr-qc].
- [98] M. Çalışkan, J. M. Ezquiaga, O. A. Hannuksela, and D. E. Holz, *Phys. Rev. D* **107**, 063023 (2023), arXiv:2201.04619 [astro-ph.CO].
- [99] A. More and S. More, *Monthly Notices of the Royal Astronomical Society* **515**, 1044 (2022).
- [100] S. van der Walt, S. C. Colbert, and G. Varoquaux, *Comput. Sci. Eng.* **13**, 22 (2011), arXiv:1102.1523 [cs.MS].
- [101] P. Virtanen *et al.*, *Nature Meth.* (2020), 10.1038/s41592-019-0686-2, arXiv:1907.10121 [cs.MS].
- [102] T. P. Robitaille *et al.*, *Astronomy & Astrophysics* **558**, A33 (2013).
- [103] A. M. Price-Whelan *et al.*, *The Astronomical Journal* **156**, 123 (2018).
- [104] J. D. Hunter, *Computing in Science & Engineering* **9**, 90 (2007).
- [105] T. Kluyver, B. Ragan-Kelley, F. Pérez, B. Granger, M. Bussonnier, J. Frederic, K. Kelley, J. Hamrick, J. Grout, S. Corlay, P. Ivanov, D. Avila, S. Abdalla, C. Willing, and J. development team, in *Positioning and Power in Academic Publishing: Players, Agents and Agendas*, edited by F. Loizides and B. Schmidt (IOS Press, Netherlands, 2016) pp. 87–90.